

Experimental Study on Additional Shields for Leakage Gamma Rays from a Duct*

By

Toshimasa MIURA ** · Kiyoshi TAKEUCHI **
and Masaharu KINNO ***

ABSTRACT

For the purpose of providing experimental data for the assessment of shielding calculations, gamma-ray dose rate distributions are measured around a rectangular shield in a concrete cavity installed at the outlet of a radiation beam hole of the research reactor JRR-4. The shield consists of concrete, iron, and lead slabs. Measurements are performed for twenty configurations which are selected from the combination of the shield slab sequence and the shield location in the cavity.

The following conclusions are obtained through the analysis of experimental data. (1) Gamma rays scattered at the duct outlet play important role in the determination of dose rates around the shield. (2) For the high energy gamma rays above 4 MeV, a better shielding effect can be obtained by setting heavier materials to the source side.

The ray-effect found in the calculation by the discrete ordinates transport code PALLAS is solved by calculating uncollided fluxes analytically. Calculations by the Monte Carlo code MORSE agree fairly well with experimental results except in the side of the shield where large inconsistencies are found.

1. INTRODUCTION

There are a large number of empty ducts in nuclear reactor shields. Since it is quite difficult to evaluate leakage radiations through ducts accurately, these irregularities present a serious problem to shield designers. It is possible to eliminate a significant fraction of leakage radiations by introducing offsets, or steps, or bends into ducts, however, additional shields are necessary to reduce leakage radiations under certain circumstances. Since ducts are equipped for the purpose of connections between radiation areas and shielded areas, such shields can not be placed in contact with duct outlets. Consequently, air gaps exist between duct outlets and additional shields. When an additional shield is a rectangular block, for example, a part of the radiations reflected from the shield surface are streaming through the

* Received on June 11, 1986

** Tokai-Branch

*** On leave from Fujita Corporation to Japan Atomic Energy Research Institute as a visiting researcher in the period of this work

gap and leak into the space around the shield. Thus, the problem includes penetration, reflection, and streaming phenomena simultaneously. Therefore it may not an easy task to evaluate the effect of additional shields satisfactorily.

In order to examine and improve calculational methods, experimental data are necessary. Also such data may be useful as a reference for the selection of materials and geometries of additional shields. For these reasons, gamma-ray dose rate distributions were measured around an experimental model of the additional shield placed in a concrete cavity. As the shield materials, concrete, iron, and lead were selected because of their different characteristics on the gamma-ray penetration and reflection.

A part of this study had been already reported in the sixth international conference on radiation shielding.⁽¹⁾ This is the final report of the study.

2. MEASUREMENTS

Measurements were carried out utilizing the Dry Shielding Test Facility of the JRR-4,⁽²⁾ a swimming-pool-type research reactor, installed at the Japan Atomic Energy Research Institute (JAERI). As shown in Fig. 1, a cubical cavity, 2.6m x 2.6m x 2.6m, was constructed at the outlet of an experimental hole with reinforced concrete panels. The front wall of the cavity has a hole of 36 cm in diameter. Three iron slabs of different sizes are

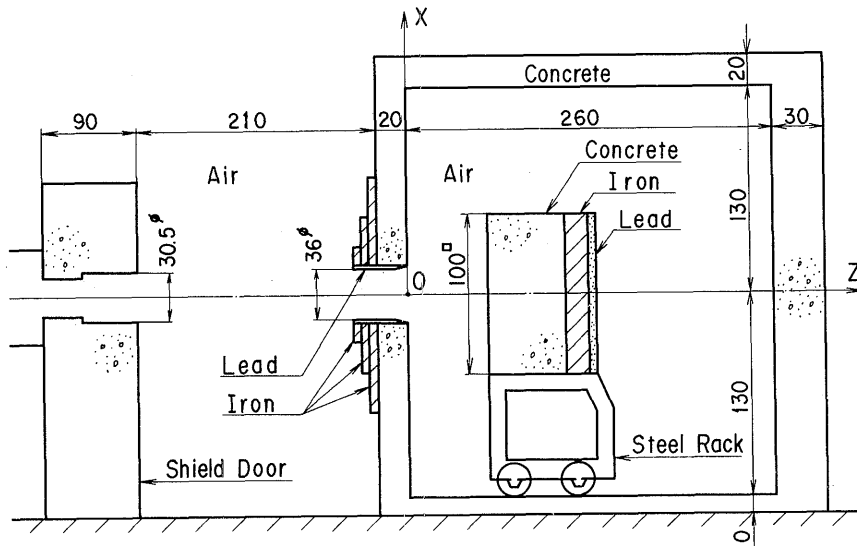


Fig. 1 Concrete cavity and a model of additional shields placed at the outlet of the experimental hole of the JRR-4. Dimensions are in centimetres.

attached to the front wall to reduce gamma rays entering into the cavity through the outer region of the hole. They are 5 cm in thickness, and 60 cm, 100 cm, and 160 cm square, respectively. Thicknesses of walls are 20 cms for the front-, the side-, and the upper-wall, 10 cm for the bottom-wall, and 30 cm for the rear-wall, respectively. Note that the floor is made of concrete.

A shield was placed in the cavity as a model of the additional shield. It has a shape of rectangular prism with a cross section of 1m x 1m and a length of 0.675m. It consists of five 10-cm-thick reinforced concrete slabs, a 15-cm-thick iron slab, and a 2.5-cm-thick lead slab. The shield was set on a steel rack. Atomic densities of the reinforced concrete used in the experiment are given in Table 1, in which values are obtained by a chemical analysis of 30-cm-long by 15-cm-diameter cylindrical concrete test pieces. The analysis was made when weights of concrete test pieces became stable. Weights of test pieces are given in Table 2 as a function of time elapsed. The value of iron in Table 1 is the one corrected for iron bars embedded in concrete. The correction increased iron percentage from 2.2 to 4.2. The

Table 1. Atomic Densities of the Reinforced Concrete

Element	Atom Density (cm^{-3})
H	1.20×10^{22}
O	4.25×10^{22}
Si	1.38×10^{22}
Al	2.74×10^{21}
Fe	^a 1.01×10^{21}
Ca	2.58×10^{21}
Mg	3.87×10^{20}
S	1.28×10^{20}
Na	8.77×10^{20}
K	6.19×10^{20}

^aCorrection is made for iron bars embedded in concrete.

Table 2. Weights of Concrete Test Pieces (g)

Sample No.	1979.11.22 ^a	1980.2.26. ^b	1980.4.2.	1981.3.26.
1	12,125	11,757	11,740	11,738
2	12,148	11,798	11,778	11,770
3	12,000	11,649	11,630	11,630

^aConcrete was made.

^bChemical analysis was performed.

measured density of the reinforced concrete is 2.27 g/cm^3 .

A cross section of the experimental hole is shown in Fig. 2. A 90-cm-thick shield door having a hole was set at the hole outlet. The hole cross sections are 30 cm square, $60 \text{ cm} \times 67.5 \text{ cm}$, 25.5 cm in diameter, and 30.5 cm in diameter from the reactor side. There exists a thick water region between the reflector and the hole inlet which attenuates neutrons effectively. Furthermore, an 1-cm-thick panel containing natural boron was inserted at the middle step of the hole to absorb slow neutrons. Thus, the effect of neutrons is considered small enough to neglect in the present gamma-ray measurements.

In measurements, sequences of shield slabs were taken as follows from the reactor side;

- (1) Concrete + Iron + Lead,
- (2) Lead + Concrete + Iron,
- (3) Iron + Concrete + Lead,
- (4) Lead + Iron + Concrete.

These shield arrangements, (1)-(4), were designated as CIL, LCI, ICL, and LIC, respectively. Shield locations were taken so that the gap width between the front wall and the shield, D , was between 10 and 90 cm. Additional two configurations were also studied, that is, no shield in the cavity with the door in the rear wall closed or open. The size of this rear door is 80 cm in width and 2.6 m in height. Except the last one, the rear door is closed in all

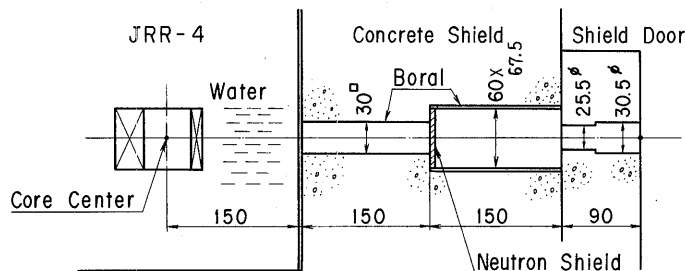


Fig. 2 Cross section of the experimental hole of the JRR-4. Dimensions are in centimetres.

Table 3. Combination of Shield Sequences and Gaps

Shield Sequence	Gap Width D (cm)					
	0	10	20	30	50	90
CIL	* ^a	*	*	*	*	*
LCI	*	—	*	—	*	*
ICL	*	—	*	—	*	*
LIC	*	—	*	—	*	*

^aMeasurements were carried out.

cases. Thus, measurements were carried out for twenty configurations. Eighteen combinations of gaps and shield sequences are given in Table 3. An example of configurations is shown in Fig. 3 together with measurement positions. Note that measurement and calculation positions will be expressed in the XYZ coordinates system of which origin is taken at the center of the inner surface of the front wall as shown in the figure.

The energy spectrum of incident gamma rays was measured at the location P_0 in Fig. 3 using a 3- x 3-in. cylindrical NaI(Tl) spectrometer before the installation of the concrete cavity. The spectrometer was set in a lead cavity box of which cross section is shown in Fig. 4. Incident gamma

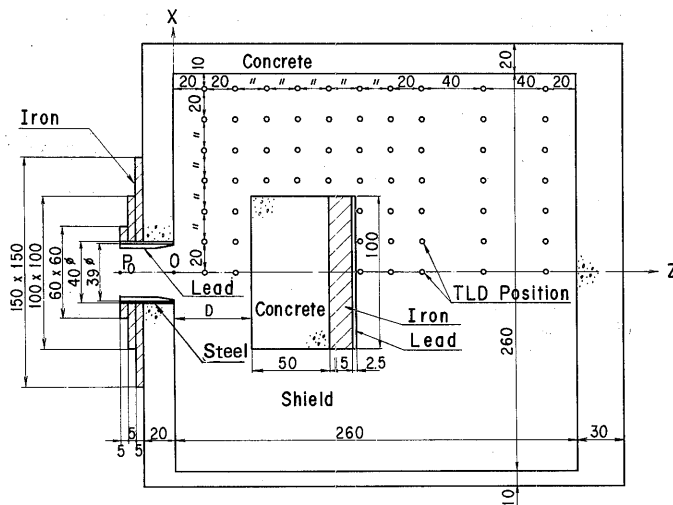


Fig. 3 An experimental configuration and measurement positions. Dimensions are in centimetres.

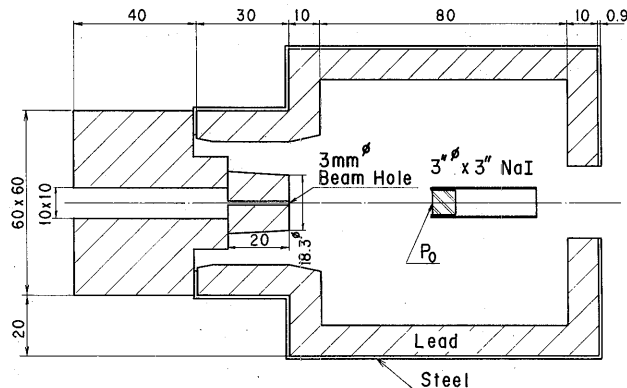


Fig. 4 Structure of the lead cavity box used in the spectrum measurement of incident gamma rays. Dimensions are in centimetres.

rays were collimated with a hole of 3 mm in diameter made in the lead shield to reduce the number of incident gamma rays and to get reasonable count rates. Thus, measurements were carried out in the reactor power range where a linear relationship was observed between dose rates at P_o and reactor powers. Response functions of the spectrometer for a collimated beam incidence were calculated with a Monte Carlo code MARTHA.⁽³⁾ Calculations were carried out taking into account the effect of the detector housing structure. The accuracy of Monte Carlo calculations was carefully examined experimentally.⁽⁴⁾ It was found that calculated response functions were accurate enough to use them in the unfolding of measured pulse height distributions. As an example, a comparison of measured and calculated ^{60}Co pulse height distributions for a collimated beam incidence is shown in

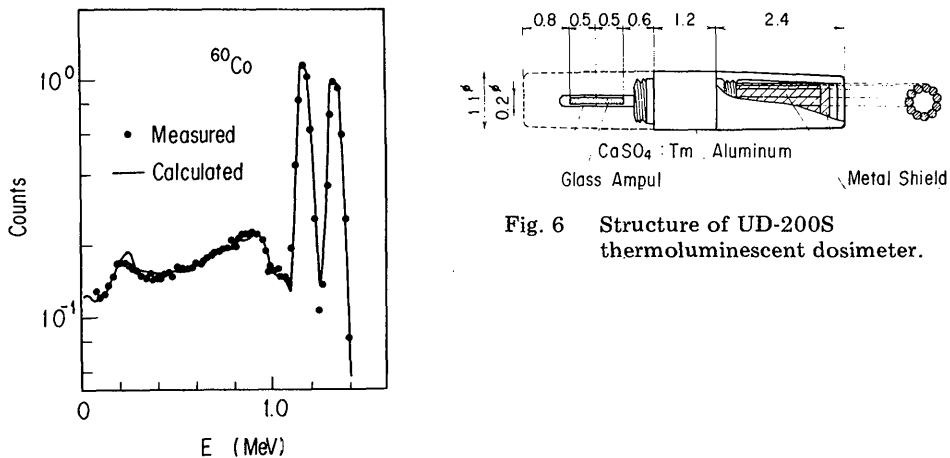


Fig. 5 Comparison of measured and calculated ^{60}Co pulse height distributions.

Table 4. Energy Spectrum of Incident Gamma Rays Measured at the Location P_o

Energy Range (MeV)	Flux ($\text{cm}^{-2} \cdot \text{sec}^{-1} \cdot \text{MeV}^{-1} \cdot \text{MW}^{-1}$)	Energy Range (MeV)	Flux ($\text{cm}^{-2} \cdot \text{sec}^{-1} \cdot \text{MeV}^{-1} \cdot \text{MW}^{-1}$)
0.0 – 0.5	4.40×10^6	4.5 – 5.0	4.35×10^6
0.5 – 1.0	3.60×10^6	5.0 – 5.5	3.46×10^6
1.0 – 1.5	4.90×10^6	5.5 – 6.0	2.15×10^6
1.5 – 2.0	1.16×10^7	6.0 – 6.5	2.04×10^6
2.0 – 2.5	1.43×10^7	6.5 – 7.0	1.55×10^6
2.5 – 3.0	8.03×10^6	7.0 – 7.5	1.36×10^6
3.0 – 3.5	1.01×10^7	7.5 – 8.0	3.36×10^6
3.5 – 4.0	6.84×10^6	8.0 – 8.5	2.05×10^5
4.0 – 4.5	7.44×10^6		

Fig. 5. Agreement is quite well. The unfolding was made with the FERDO code.⁽⁵⁾ An unfolded spectrum is given in Table 4 for a reactor power of 1 MW. A X-directional dose rate distribution of incident gamma rays was measured on a traverse intersecting the point P_o shown in Fig. 3. The result is given in Table 5.

Gamma-ray dose rate distributions were measured two-dimensionally on the XZ plane at Y = 0 cm in the cavity. Measurements were carried out by using thermoluminescent dosimeters (TLD) and a TLD reader. They are type UD-200S dosimeters and a UD-505A reader produced by Matsushita Electric Co. Ltd. The structure of the UD-200S dosimeter is shown in Fig. 6. Two glass capsules containing CaSO₄(Tm) powder are covered with shielding caps made of an alloy so as to make the detector response for gamma rays approximately flat above about 30 keV. The relative energy response of the UD-200S thermoluminescent dosimeter is shown in Fig. 7. The detector calibration was carried out by using a ⁶⁰Co standard source. Conversion factors from readings to dose rates are shown in Fig. 8.

In the cavity, strings were stretched from the ceiling to the floor vertically. TLDs were kept on the strings with adhesive tapes so that their axes were parallel to the strings. Irradiations of TLDs were made for about 5 minutes at 200 kW or for 2 to 6 hours at 3.5 MW depending on dose rates expected at each measurement position. After irradiations, TLDs were kept in a lead box for more than two days and then measured. These measurements by a NaI(Tl) detector and TLDs were carried out in the reactor power range of 1 kW to 3.5 MW. A linear relationship between gamma-ray dose rates and reactor powers is seen above about 1 kW at the outlet of the experimental hole, as shown in Fig. 9.

Table 5. X-Directional Dose Rate Distribution Measured at the Location P_o

X (cm)	Dose Rate	X (cm)	Dose Rate
0.0	1.0	11.0	0.87
1.0	1.0	12.0	0.84
2.0	1.0	13.0	0.83
3.0	1.0	14.0	0.79
4.0	0.98	15.0	0.76
5.0	0.97	16.0	0.72
6.0	0.96	17.0	0.68
7.0	0.95	18.0	0.63
8.0	0.92	19.0	0.49
9.0	0.91	20.0	0.32
10.0	0.90	21.0	0.097
		22.0	0.026

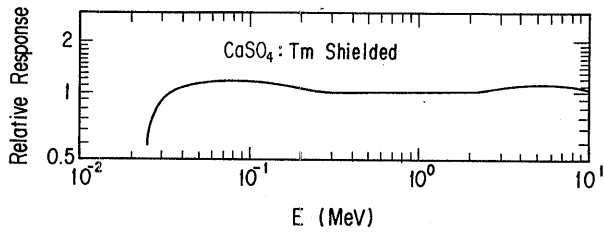


Fig. 7 Relative energy response of UD-200S thermoluminescent dosimeter.

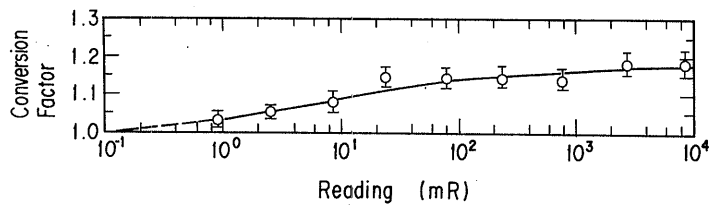


Fig. 8 Conversion factors from readings to dose rates measured for UD-200S thermoluminescent dosimeter.

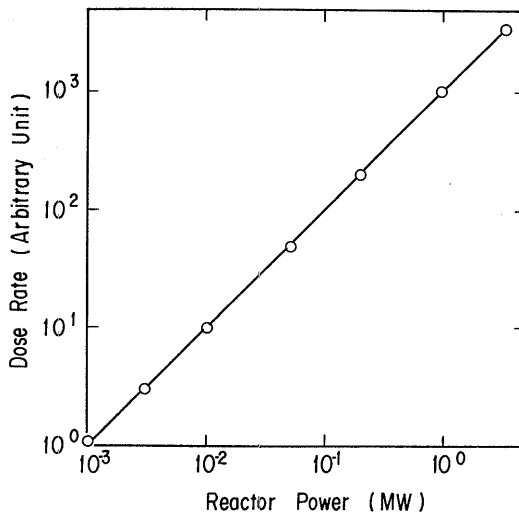


Fig. 9 Relationship between dose rates of incident gamma rays and reactor powers.

3. ANALYSIS OF EXPERIMENTAL RESULTS

Dose rates measured in the cavity are given in Tables 6-25 in units of $\text{mR} \times \text{h}^{-1} \times \text{MW}^{-1}$. Each value in Tables is an average of those measured by two capsules of a UD-200S detector. Tables 6-11 are for CILs, Tables 12-15 are for LCIs, Tables 16-19 are for ICLs, and Tables 20-23 are for LICs, respectively. Tables 24 and 25 are for the cases of no shield in the cavity with the rear door closed or open. Contour maps of dose rates are shown in

Table 6. Dose Rate Measured in the CIL Configuration of $D = 0$ cm
($\text{mR} \times \text{h}^{-1} \times \text{MW}^{-1}$)

Z (cm)	X (cm)						
	0	20	40	60	80	100	120
20	—	—	—	$6.65 + 0^a$	$3.49 + 0$	$2.16 + 0$	$1.68 + 0$
40	—	—	—	$7.93 + 0$	$3.94 + 0$	$2.75 + 0$	$1.91 + 0$
60	—	—	—	$4.02 + 0$	$3.57 + 0$	$2.55 + 0$	$1.84 + 0$
80	$8.28 + 1$	$3.86 + 1$	$1.45 + 0$	$6.71 - 1$	$1.77 + 0$	$1.97 + 0$	$1.66 + 0$
100	$5.59 + 1$	$3.39 + 1$	$4.12 + 0$	$1.05 + 0$	$9.41 - 1$	$1.24 + 0$	$1.27 + 0$
120	$4.15 + 1$	$2.96 + 1$	$5.46 + 0$	$1.69 + 0$	$9.86 - 1$	$9.48 - 1$	$9.39 - 1$
140	$2.99 + 1$	$2.41 + 1$	$5.93 + 0$	$2.16 + 0$	$1.07 + 0$	$8.44 - 1$	$7.57 - 1$
160	$2.53 + 1$	$2.14 + 1$	$5.57 + 0$	$2.21 + 0$	$1.24 + 0$	$8.02 - 1$	$6.96 - 1$
200	$1.99 + 1$	$1.75 + 1$	$4.61 + 0$	$2.66 + 0$	$1.51 + 0$	$8.87 - 1$	$7.25 - 1$
240	$1.55 + 1$	$1.55 + 1$	$3.84 + 0$	$2.49 + 0$	$1.58 + 0$	$1.04 + 0$	$7.33 - 1$
290	$3.55 + 0$	$3.64 + 0$	$6.02 - 1$	$3.52 - 1$	$2.02 - 1$	$1.24 - 1$	$7.57 - 2$

^aRead as 6.65×10^0

Table 7. Dose Rate Measured in the CIL Configuration of $D = 10$ cm
($\text{mR} \times \text{h}^{-1} \times \text{MW}^{-1}$)

Z (cm)	X (cm)						
	0	20	40	60	80	100	120
5	$1.60 + 5^a$	$5.33 + 4$	$2.22 + 2$	$4.83 + 1$	$1.73 + 1$	$9.48 + 0$	$3.31 + 0$
20	—	—	—	$9.67 + 0$	$7.88 + 0$	$5.59 + 0$	$4.88 + 0$
40	—	—	—	$9.36 + 0$	$5.91 + 0$	$4.44 + 0$	$3.18 + 0$
60	—	—	—	$7.39 + 0$	$5.20 + 0$	$3.43 + 0$	$2.80 + 0$
80	—	—	—	$1.43 + 0$	$2.99 + 0$	$2.89 + 0$	$2.26 + 0$
100	$6.47 + 1$	$3.23 + 1$	$2.99 + 0$	$1.08 + 0$	$1.38 + 0$	$1.95 + 0$	$2.05 + 0$
120	$4.46 + 1$	$2.95 + 1$	$5.08 + 0$	$1.63 + 0$	$1.10 + 0$	$1.26 + 0$	$1.47 + 0$
160	$2.68 + 1$	$2.28 + 1$	$5.49 + 0$	$2.49 + 0$	$1.26 + 0$	$9.55 - 1$	$8.66 - 1$
200	$1.88 + 1$	$1.84 + 1$	$4.76 + 0$	$2.69 + 0$	$1.53 + 0$	$1.03 + 0$	$8.21 - 1$
240	$1.58 + 1$	$1.49 + 1$	$3.75 + 0$	$2.37 + 0$	$1.62 + 0$	$1.12 + 0$	$8.08 - 1$

^aRead as 1.60×10^5

Figs. 10-14 for all configurations except the cases of $D = 10$ and 30 cm for CIL arrangements.

Experimental errors in the absolute magnitude of measured dose rates are due to the variation of the reactor power, the uncertainty of the irradiation time and the location of the detector, the statistical error in the TLD calibration, and the uncertainty arising from the change of the TLD response which depends on the incident angle and the energy of gamma rays. The error due to the variation of the reactor power is measured less than 2 percent. The uncertainty in the irradiation time is slightly large for the posi-

Table 8. Dose Rate Measured in the CIL Configuration of $D = 20$ cm ($\text{mR} \times \text{h}^{-1} \times \text{MW}^{-1}$)

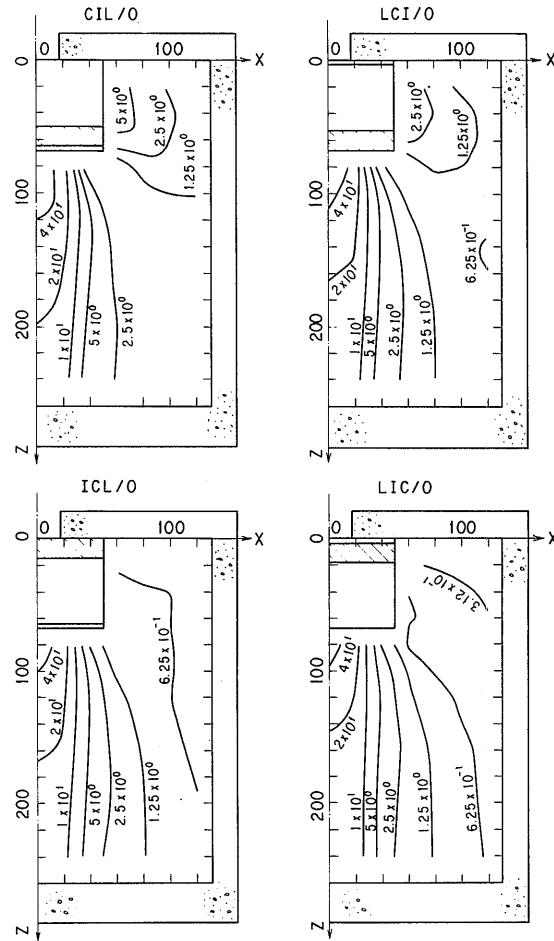
Z (cm)	X (cm)						
	0	20	40	60	80	100	120
10	$1.62 + 5^a$	$5.11 + 4$	$3.03 + 2$	$8.60 + 1$	$3.42 + 1$	$2.00 + 1$	$1.02 + 1$
20	—	—	—	$4.74 + 1$	$1.82 + 1$	$1.02 + 1$	$7.56 + 0$
40	—	—	—	$1.27 + 1$	$1.22 + 1$	$1.07 + 1$	$8.84 + 0$
60	—	—	—	$1.16 + 1$	$8.39 + 0$	$6.49 + 0$	$6.39 + 0$
80	—	—	—	$5.04 + 0$	$5.67 + 0$	$5.05 + 0$	$4.30 + 0$
100	$7.40 + 1$	$4.41 + 1$	$1.67 + 0$	$1.46 + 0$	$3.16 + 0$	$3.45 + 0$	$3.21 + 0$
120	$4.95 + 1$	$3.63 + 1$	$4.86 + 0$	$1.69 + 0$	$1.73 + 0$	$2.18 + 0$	$2.46 + 0$
160	$3.02 + 1$	$2.47 + 1$	$5.80 + 0$	$2.68 + 0$	$1.57 + 0$	$1.22 + 0$	$1.32 + 0$
200	$2.11 + 1$	$1.99 + 1$	$5.49 + 0$	$2.94 + 0$	$1.73 + 0$	$1.23 + 0$	$1.06 + 0$
240	$1.62 + 1$	$1.54 + 1$	$4.55 + 0$	$2.52 + 0$	$1.79 + 0$	$1.24 + 0$	$9.92 - 1$

^aRead as 1.62×10^5

Table 9. Dose Rate Measured in the CIL Configuration of $D = 30$ cm ($\text{mR} \times \text{h}^{-1} \times \text{MW}^{-1}$)

Z (cm)	X (cm)						
	0	20	40	60	80	100	120
10	$1.67 + 5^a$	$8.66 + 3$	$3.24 + 2$	$1.19 + 2$	$5.29 + 1$	$2.89 + 1$	$1.70 + 1$
20	$1.48 + 5$	$2.65 + 4$	$3.86 + 2$	$1.06 + 2$	$4.23 + 1$	$2.21 + 1$	$1.40 + 1$
40	—	—	—	$2.25 + 1$	$2.96 + 1$	$1.79 + 1$	$1.06 + 1$
60	—	—	—	$1.52 + 1$	$1.42 + 1$	$1.49 + 1$	$1.38 + 1$
80	—	—	—	$9.95 + 0$	$9.11 + 0$	$8.25 + 0$	$7.91 + 0$
100	$8.03 + 1$	$4.56 + 1$	$6.54 - 1$	$2.57 + 0$	$5.53 + 0$	$5.59 + 0$	$5.88 + 0$
120	$6.54 + 1$	$3.75 + 1$	$3.52 + 0$	$1.98 + 0$	$2.78 + 0$	$4.16 + 0$	$4.37 + 0$
160	$3.57 + 1$	$2.48 + 1$	$6.14 + 0$	$2.79 + 0$	$2.05 + 0$	$2.02 + 0$	$2.26 + 0$
200	$2.44 + 1$	$2.11 + 1$	$5.84 + 0$	$3.29 + 0$	$2.14 + 0$	$1.69 + 0$	$1.60 + 0$
240	$1.74 + 1$	$1.75 + 1$	$5.45 + 0$	$3.15 + 0$	$1.92 + 0$	$1.69 + 0$	$1.25 + 0$

^aRead as 1.67×10^5



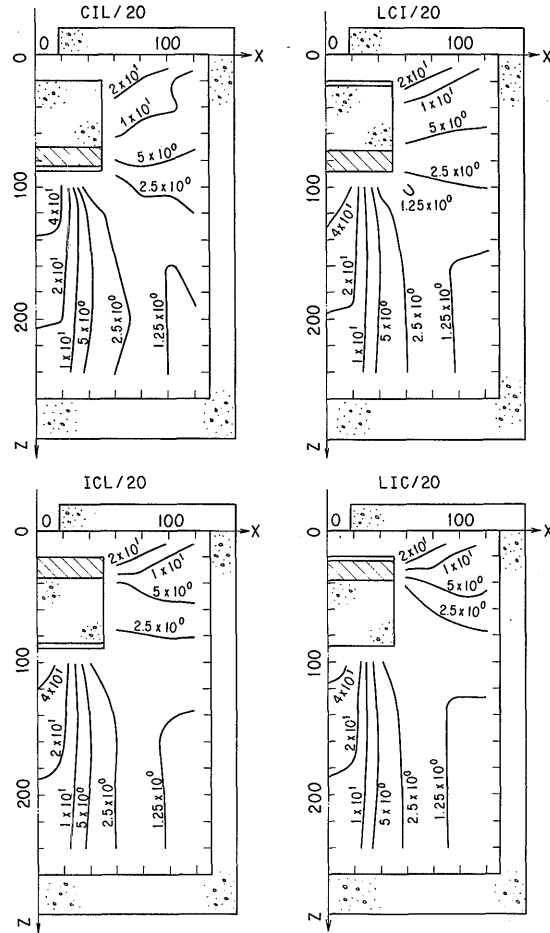


Fig. 11 Contour maps of dose rates measured in four configurations of the gap width, $D = 20$ cm. Units of dose rates are $\text{mR} \times \text{h}^{-1} \times \text{MW}^{-1}$. Dimensions are in centimetres.

Table 11. Dose Rate Measured in the CIL Configuration of $D = 90$ cm ($\text{MR} \times \text{h}^{-1} \times \text{MW}^{-1}$)

Z (cm)	X (cm)						
	0	20	40	60	80	100	120
20	$1.47 + 5^a$	$2.41 + 4$	$2.76 + 2$	$1.01 + 1$	$5.82 + 1$	$4.11 + 1$	$3.26 + 1$
40	$1.40 + 5$	$4.84 + 4$	$4.67 + 2$	$1.60 + 2$	$8.09 + 1$	$4.59 + 1$	$3.22 + 1$
60	$1.21 + 5$	$4.67 + 4$	$5.97 + 2$	$2.37 + 2$	$9.92 + 1$	$5.42 + 1$	$3.23 + 1$
80	$1.31 + 5$	$4.90 + 4$	$6.66 + 2$	$1.80 + 2$	$7.81 + 1$	$4.21 + 1$	$2.35 + 1$
100	—	—	—	$6.39 + 1$	$8.08 + 1$	$3.60 + 1$	$2.60 + 1$
120	—	—	—	$2.71 + 1$	$5.41 + 1$	$5.18 + 1$	$3.34 + 1$
140	—	—	—	$1.63 + 1$	$3.22 + 1$	$4.08 + 1$	$3.21 + 1$
160	$6.61 + 1$	$5.11 + 1$	$1.11 + 0$	$5.11 + 0$	$1.61 + 1$	$3.21 + 1$	$3.03 + 1$
180	$5.65 + 1$	$4.09 + 1$	$4.62 + 0$	$3.29 + 0$	$8.09 + 0$	$1.97 + 1$	$2.41 + 1$
200	$4.19 + 1$	$3.17 + 1$	$6.72 + 0$	$3.46 + 0$	$4.97 + 0$	$1.09 + 1$	$1.85 + 1$
240	$2.68 + 1$	$2.56 + 1$	$7.37 + 0$	$3.62 + 0$	$3.77 + 0$	$5.25 + 0$	$8.19 + 0$

(128)

^a Read as 1.47×10^5

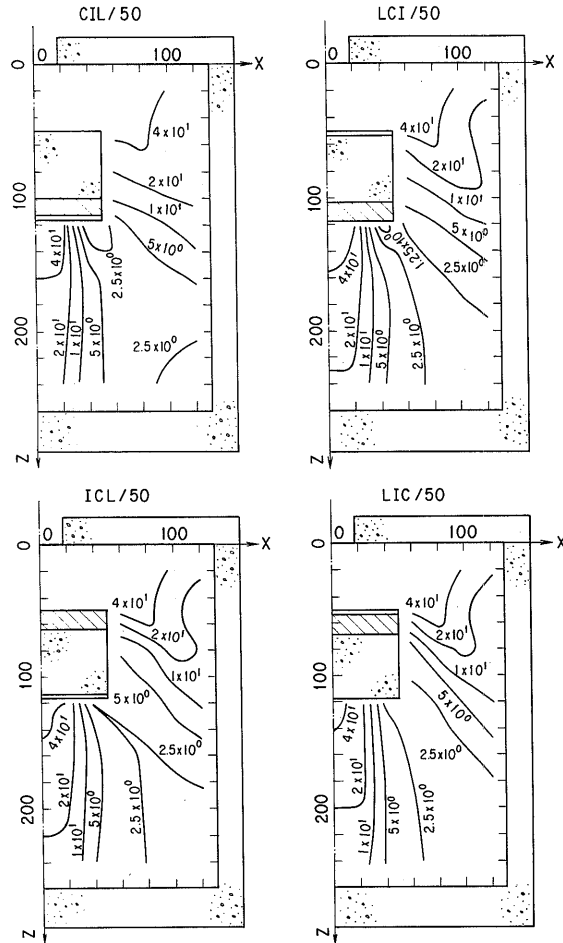


Fig. 12 Contour maps of dose rates measured in four configurations of the gap width, $D = 50$ cm. Units of dose rates are $\text{mR} \times \text{h}^{-1} \times \text{MW}^{-1}$. Dimensions are in centimetres.

Table 12. Dose Rate Measured in the LCI Configuration of $D = 0$ cm ($\text{mR} \times \text{h}^{-1} \times \text{MW}^{-1}$)

Z (cm)	X (cm)						
	0	20	40	60	80	100	120
20	—	—	—	$3.86 + 0^a$	$1.91 + 0$	$1.08 + 0$	$8.15 - 1$
40	—	—	—	$4.55 + 0$	$2.50 + 0$	$1.64 + 0$	$1.03 + 0$
60	—	—	—	$2.70 + 0$	$2.24 + 0$	$1.58 + 0$	$1.10 + 0$
80	$6.51 + 1$	$3.39 + 1$	$1.53 + 0$	$6.08 - 1$	$1.41 + 0$	$1.27 + 0$	$1.02 + 0$
100	$5.01 + 1$	$2.75 + 1$	$3.76 + 0$	$9.85 - 1$	$8.35 - 1$	$9.48 - 1$	$9.24 - 1$
120	$3.38 + 1$	$2.41 + 1$	$4.72 + 0$	$1.43 + 0$	$8.53 - 1$	$7.53 - 1$	$7.17 - 1$
140	$2.68 + 1$	$2.10 + 1$	$4.53 + 0$	$1.86 + 0$	$9.72 - 1$	$7.35 - 1$	$5.72 - 1$
160	$2.09 + 1$	$1.84 + 1$	$4.64 + 0$	$2.09 + 0$	$1.06 + 0$	$7.60 - 1$	$6.10 - 1$
200	$1.54 + 1$	$1.54 + 1$	$4.40 + 0$	$2.27 + 0$	$1.29 + 0$	$7.52 - 1$	$6.43 - 1$
240	$1.44 + 1$	$1.42 + 1$	$3.37 + 0$	$2.22 + 0$	$1.27 + 0$	$8.79 - 1$	$6.48 - 1$
290	$3.27 + 0$	$3.30 + 0$	$5.26 - 1$	$3.00 - 1$	$1.84 - 1$	$1.05 - 1$	$6.96 - 2$

^a Read as 3.86×10^0

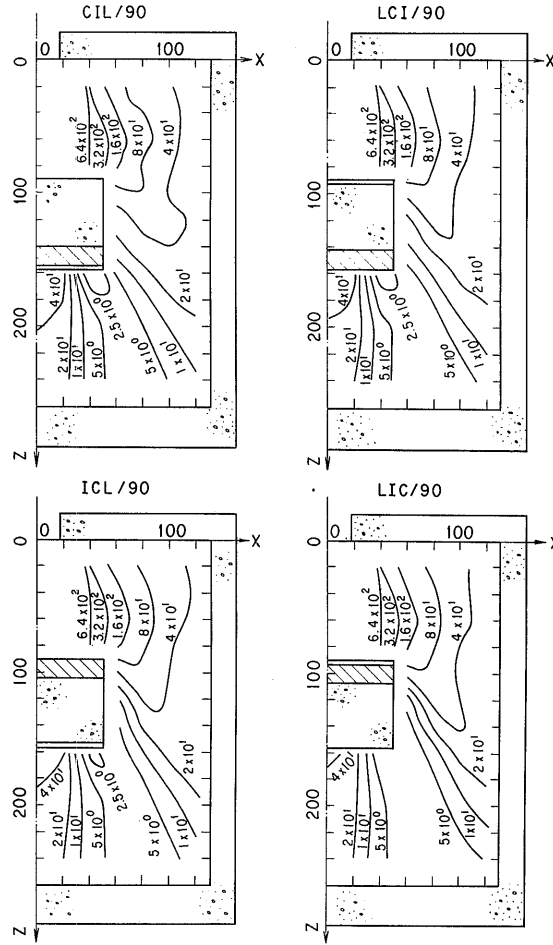


Fig. 13 Contour maps of dose rates measured in four configurations of the gap width, $D = 90$ cm. Units of dose rates are $mR \times h^{-1} \times MW^{-1}$. Dimensions are in centimetres.

Table 13. Dose Rate Measured in the LCI Configuration of $D = 20$ cm ($mR \times h^{-1} \times MW^{-1}$)

Z (cm)	X (cm)						
	0	20	40	60	80	100	120
10	$1.60 + 5^a$	$6.38 + 3$	$2.86 + 2$	$6.97 + 1$	$2.99 + 1$	$1.59 + 1$	$8.54 + 0$
20	—	—	—	$3.38 + 1$	$1.42 + 1$	$8.60 + 0$	$5.45 + 0$
40	—	—	—	$6.88 + 0$	$6.60 + 0$	$7.11 + 0$	$7.14 + 0$
60	—	—	—	$6.22 + 0$	$5.19 + 0$	$4.66 + 0$	$4.45 + 0$
80	—	—	—	$3.65 + 0$	$3.40 + 0$	$3.37 + 0$	$2.94 + 0$
100	$7.07 + 1$	$3.84 + 1$	$1.97 + 0$	$1.15 + 0$	$2.20 + 0$	$2.43 + 0$	$2.56 + 0$
120	$4.63 + 1$	$2.96 + 1$	$4.05 + 0$	$1.53 + 0$	$1.46 + 0$	$1.79 + 0$	$1.87 + 0$
160	$2.83 + 1$	$2.23 + 1$	$5.15 + 0$	$2.13 + 0$	$1.38 + 0$	$1.18 + 0$	$1.03 + 0$
200	$1.87 + 1$	$1.87 + 1$	$4.76 + 0$	$2.48 + 0$	$1.54 + 0$	$1.17 + 0$	$9.62 - 1$
240	$1.64 + 1$	$1.65 + 1$	$4.14 + 0$	$2.54 + 0$	$1.61 + 0$	$1.19 + 0$	$9.43 - 1$

(130)

^a Read as 1.60×10^5

tions on the lines $X = 0$ and 20 cm in front of the shield where short irradiation time was taken. It is less than 6 percent. In other positions, it is less than 0.3 percent. The uncertainty in the detector location is less than 2 mm in the X-direction and less than 6 mm in the Y- or Z-direction, which results in different magnitude of the error depending on the spatial distribution of dose rates around measurement positions. For example, the uncertainty of 6 mm in the detector location results in 2, 4, and 9 percent error where dose rates change 2-, 4-, and 8-fold by each 20 cm, respectively. This error is, in general, less than 4 percent except the positions on the lines

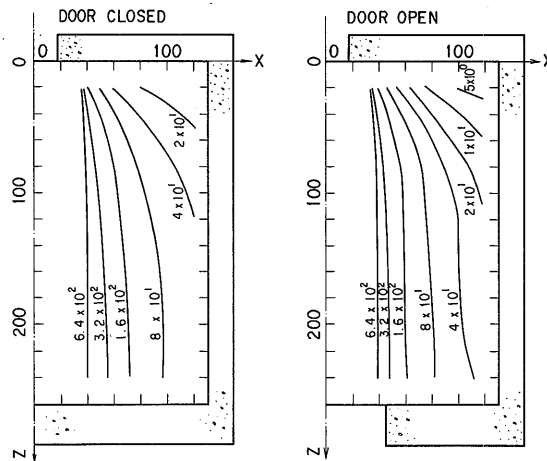


Fig. 14 Contour maps of dose rates measured in two configurations with the rear door closed or open. Units of dose rates are $\text{mR} \times \text{h}^{-1} \times \text{MW}^{-1}$. Dimensions are in centimetres.

Table 14. Dose Rate Measured in the LCI Configuration of $D = 50$ cm ($\text{mR} \times \text{h}^{-1} \times \text{MW}^{-1}$)

Z (cm)	X (cm)						
	0	20	40	60	80	100	120
20	$1.50 + 5^a$	$2.38 + 4$	$4.31 + 2$	$1.37 + 2$	$5.93 + 1$	$3.42 + 1$	$2.26 + 1$
40	$1.40 + 5$	$4.24 + 4$	$4.93 + 2$	$1.20 + 2$	$4.80 + 1$	$2.32 + 1$	$1.52 + 1$
60	—	—	—	$2.32 + 1$	$4.45 + 1$	$2.41 + 1$	$1.47 + 1$
80	—	—	—	$1.12 + 1$	$2.13 + 1$	$2.61 + 1$	$1.82 + 1$
100	—	—	—	$7.06 + 0$	$8.53 + 0$	$1.72 + 1$	$1.80 + 1$
120	$7.54 + 1$	$4.26 + 1$	$9.14 - 1$	$2.85 + 0$	$4.63 + 0$	$7.23 + 0$	$1.05 + 1$
140	$5.37 + 1$	$3.62 + 1$	$3.70 + 0$	$2.02 + 0$	$3.10 + 0$	$4.43 + 0$	$6.24 + 0$
160	$3.64 + 1$	$2.91 + 1$	$5.69 + 0$	$2.39 + 0$	$2.16 + 0$	$2.90 + 0$	$3.68 + 0$
200	$2.42 + 1$	$2.17 + 1$	$6.16 + 0$	$3.01 + 0$	$2.08 + 0$	$1.91 + 0$	$2.18 + 0$
240	$1.88 + 1$	$1.88 + 1$	$5.55 + 0$	$3.15 + 0$	$2.18 + 0$	$1.80 + 0$	$1.64 + 0$

^aRead as 1.50×10^5

of X = 20 and 40 cm in front of the shield where steep gradient of dose rates are seen.

As shown in Fig. 8, the TLD calibration was carried out for nine doses. These doses were obtained by adjusting detector locations to the source and irradiation time. For each dose, five detectors, that is, ten capsules, were irradiated. Standard deviations in conversion factors from readings to doses vary from 3.2 to 6.8 percent depending on the measured dose. Most of these

Table 15. Dose Rate Measured in the LCI Configuration of D = 90 cm
(mR × h⁻¹ × MW⁻¹)

Z (cm)	X (cm)						
	0	20	40	60	80	100	120
20	1.52 + 5 ^a	2.28 + 4	2.75 + 2	1.15 + 2	7.02 + 1	4.85 + 1	3.18 + 1
40	1.28 + 5	4.22 + 4	4.65 + 2	1.79 + 2	8.06 + 1	4.71 + 1	3.16 + 1
60	1.15 + 5	4.72 + 4	5.88 + 2	2.16 + 2	9.31 + 1	4.96 + 1	2.85 + 1
80	1.11 + 5	4.71 + 4	6.54 + 2	1.79 + 2	7.65 + 1	4.23 + 1	2.17 + 1
100	—	—	—	4.87 + 1	5.78 + 1	3.50 + 1	2.03 + 1
120	—	—	—	1.68 + 1	5.71 + 1	3.41 + 1	2.39 + 1
140	—	—	—	9.27 + 0	2.75 + 1	3.37 + 1	2.79 + 1
160	6.95 + 1	4.10 + 1	1.36 + 0	3.70 + 0	1.09 + 1	2.78 + 1	2.72 + 1
180	5.37 + 1	3.83 + 1	3.76 + 0	2.63 + 0	5.37 + 0	1.61 + 1	2.14 + 1
200	3.40 + 1	2.96 + 1	6.39 + 0	3.62 + 0	3.62 + 0	8.64 + 0	1.55 + 1
240	2.25 + 1	2.05 + 1	5.96 + 0	3.57 + 0	3.00 + 0	3.58 + 0	6.72 + 0

^aRead as 1.52×10^5

Table 16. Dose Rate Measured in the ICL Configuration of D = 0 cm
(mR × h⁻¹ × MW⁻¹)

Z (cm)	X (cm)						
	0	20	40	60	80	100	120
20	—	—	—	5.78 - 1 ^a	3.42 - 1	1.66 - 1	1.64 - 1
40	—	—	—	1.08 + 0	7.51 - 1	6.44 - 1	4.65 - 1
60	—	—	—	1.10 + 0	8.51 - 1	6.12 - 1	3.66 - 1
80	6.16 + 1	3.15 + 1	2.02 + 0	6.39 - 1	7.34 - 1	6.43 - 1	4.50 - 1
100	4.26 + 1	2.61 + 1	4.03 + 0	9.79 - 1	6.47 - 1	6.33 - 1	5.67 - 1
120	3.18 + 1	2.18 + 1	4.54 + 0	1.51 + 0	7.75 - 1	6.22 - 1	6.08 - 1
140	2.64 + 1	2.13 + 1	4.74 + 0	1.76 + 0	1.08 + 0	6.77 - 1	5.47 - 1
160	2.11 + 1	1.90 + 1	4.69 + 0	1.97 + 0	1.12 + 0	7.39 - 1	5.46 - 1
200	1.63 + 1	1.52 + 1	4.16 + 0	2.21 + 0	1.23 + 0	7.83 - 1	6.54 - 1
240	1.36 + 1	1.35 + 1	3.06 + 0	1.99 + 0	1.27 + 0	8.21 - 1	6.33 - 1
290	3.41 + 0	3.33 + 0	4.84 - 1	2.98 - 1	1.79 - 1	1.16 - 1	6.91 - 2

^aRead as 5.78×10^{-1}

deviations are considered due to the lack of the uniformity among detectors. The sensitivity of the UD-200S detector depends on the energy and the angle of incident gamma rays. The relative energy response is about 1.0 between 0.3 and 2 MeV and slightly higher than 1.0 in other energy regions except below about 30 keV. Since the TLD calibration was made by using a ^{60}Co source which emits 1.17 and 1.33 MeV gamma rays, measured dose rates must be larger than true values when gamma-ray energy spectra have their components in the energy region above 2 MeV or below 0.3 MeV. Meanwhile, dominant components of incident gamma rays exist between 1.5 and

Table 17. Dose Rate Measured in the ICL Configuration of D = 20 cm
(mR \times h $^{-1}$ \times MW $^{-1}$)

Z (cm)	X (cm)						
	0	20	40	60	80	100	120
10	1.58 + 5 ^a	6.44 + 3	2.57 + 2	7.54 + 1	3.31 + 1	1.80 + 1	9.51 + 0
20	—	—	—	4.04 + 1	1.62 + 1	8.98 + 0	6.40 + 0
40	—	—	—	3.86 + 0	6.23 + 0	7.79 + 0	7.72 + 0
60	—	—	—	2.78 + 0	3.29 + 0	3.82 + 0	3.97 + 0
80	—	—	—	2.34 + 0	2.39 + 0	2.53 + 0	2.50 + 0
100	5.88 + 1	3.41 + 1	2.58 + 0	1.38 + 0	1.83 + 0	1.89 + 0	1.82 + 0
120	4.06 + 1	2.75 + 1	4.37 + 0	1.78 + 0	1.44 + 0	1.40 + 0	1.45 + 0
160	2.58 + 1	2.07 + 1	5.22 + 0	2.55 + 0	1.47 + 0	1.12 + 0	9.64 - 1
200	1.81 + 1	1.76 + 1	4.77 + 0	2.39 + 0	1.64 + 0	1.18 + 0	9.31 - 1
240	1.51 + 1	1.57 + 1	3.93 + 0	2.44 + 0	1.65 + 0	1.16 + 0	9.86 - 1

^aRead as 1.58×10^5

Table 18. Dose Rate Measured in the ICL Configuration of D = 50 cm
(mR \times h $^{-1}$ \times MW $^{-1}$)

Z (cm)	X (cm)						
	0	20	40	60	80	100	120
20	1.54 + 5 ^a	3.44 + 4	3.93 + 2	1.36 + 2	6.06 + 1	3.65 + 1	2.46 + 1
40	1.45 + 5	4.50 + 4	4.82 + 2	1.32 + 2	5.16 + 1	2.41 + 1	1.52 + 1
60	—	—	—	2.12 + 1	4.82 + 1	2.29 + 1	1.58 + 1
80	—	—	—	5.58 + 0	1.97 + 1	2.56 + 1	1.92 + 1
100	—	—	—	3.88 + 0	5.94 + 0	1.33 + 1	1.45 + 1
120	6.00 + 1	4.02 + 1	1.61 + 0	3.08 + 0	3.44 + 0	6.43 + 0	1.18 + 1
140	4.60 + 1	3.29 + 1	4.67 + 0	2.40 + 0	2.94 + 0	4.25 + 0	6.09 + 0
160	3.25 + 1	2.60 + 1	5.84 + 0	2.78 + 0	2.39 + 0	2.75 + 0	3.69 + 0
200	2.20 + 1	2.07 + 1	5.71 + 0	3.16 + 0	2.20 + 0	2.15 + 0	2.03 + 0
240	1.84 + 1	1.77 + 1	5.12 + 0	3.19 + 0	2.37 + 0	1.88 + 0	1.74 + 0

^aRead as 1.54×10^5

5 MeV and gamma rays penetrated the shield have the energy spectrum harder than that of incident gamma rays, as shown below by one-dimensional transport calculations by the PALLAS code.⁽⁶⁾ Therefore the measured dose rates on the lines X = 0 and 20 cm must be overestimated, however, this overestimation is less than 10 percent. In the region of X > 40 cm where scattered gamma rays are dominant, the error can be considered less than 5 percent from the spectra obtained by two-dimensional transport

Table 19. Dose Rate Measured in the ICL Configuration of D = 90 cm
(mR x h⁻¹ x MW⁻¹)

Z (cm)	X (cm)						
	0	20	40	60	80	100	120
20	1.62 + 5 ^a	3.15 + 4	2.92 + 2	1.14 + 2	6.97 + 1	4.76 + 1	3.45 + 1
40	1.44 + 5	3.94 + 4	4.79 + 2	1.84 + 2	9.13 + 1	5.24 + 1	3.64 + 1
60	1.34 + 5	5.19 + 4	6.41 + 2	2.30 + 2	1.06 + 2	5.42 + 1	3.38 + 1
80	1.23 + 5	5.67 + 4	5.61 + 2	1.77 + 2	9.22 + 2	4.16 + 1	2.78 + 1
100	—	—	—	4.01 + 1	6.22 + 1	3.86 + 1	2.28 + 1
120	—	—	—	7.78 + 0	4.80 + 1	3.87 + 1	2.56 + 1
140	—	—	—	4.84 + 0	2.50 + 1	3.62 + 1	3.14 + 1
160	5.91 + 1	4.27 + 1	2.05 + 0	3.37 + 0	9.97 + 0	2.99 + 1	3.14 + 1
180	4.54 + 1	3.30 + 1	5.11 + 0	2.87 + 0	5.02 + 0	1.56 + 1	2.45 + 1
200	3.38 + 1	2.74 + 1	6.79 + 0	3.70 + 0	3.72 + 0	7.40 + 0	1.84 + 1
240	2.14 + 1	2.12 + 1	6.79 + 0	3.99 + 0	3.34 + 0	3.96 + 0	6.78 + 0

^aRead as 1.62 x 10⁵

Table 20. Dose Rate Measured in the LIC Configuration of D = 0 cm
(mR x h⁻¹ x MW⁻¹)

Z (cm)	X (cm)						
	0	20	40	60	80	100	120
20	—	—	—	3.46 - 1 ^a	2.89 - 1	1.95 - 1	1.46 - 1
40	—	—	—	6.34 - 1	5.42 - 1	4.28 - 1	2.60 - 1
60	—	—	—	6.51 - 1	5.79 - 1	4.42 - 1	3.45 - 1
80	4.98 + 1	2.96 + 1	2.29 + 0	5.64 - 1	6.01 - 1	4.94 - 1	3.70 - 1
100	3.85 + 1	2.17 + 1	3.77 + 0	1.13 + 0	5.97 - 1	5.42 - 1	4.83 - 1
120	2.65 + 1	1.96 + 1	4.31 + 0	1.35 + 0	7.29 - 1	5.63 - 1	4.61 - 1
140	2.13 + 1	1.79 + 1	4.32 + 0	1.75 + 0	8.84 - 1	6.27 - 1	4.21 - 1
160	1.81 + 1	1.73 + 1	4.10 + 0	1.97 + 0	1.01 + 0	7.11 - 1	5.25 - 1
200	1.54 + 1	1.50 + 1	3.69 + 0	1.94 + 0	1.13 + 0	6.82 - 1	5.82 - 1
240	1.37 + 1	1.34 + 1	3.16 + 0	1.98 + 0	1.13 + 0	7.74 - 1	5.88 - 1
290	3.01 + 0	3.14 + 0	4.58 - 1	2.75 - 1	1.70 - 1	1.05 - 1	6.48 - 2

^aRead as 3.46 x 10⁻¹

calculations. However the error increases to more than 10 percent around the position of $Z = 20$ cm and $X = 120$ cm where most of gamma rays have energies less than 500 keV.

Since the UD-200S dosimeter is covered with cylindrical metal shields, the sensitivity varies depending on the incident angle of gamma rays. The angle dependent sensitivity was measured by using a ^{60}Co source. It was almost constant except near the axial incidence for which it was about 14 percent lower. Thus, it is considered that the error arising from the angle dependent sensitivity is small and it is neglected. As a whole, the experi-

Table 21. Dose Rate Measured in the LIC Configuration of $D = 20$ cm
($\text{mR} \times \text{h}^{-1} \times \text{MW}^{-1}$)

Z (cm)	X (cm)						
	0	20	40	60	80	100	120
10	$1.48 + 5^a$	$1.01 + 4$	$2.94 + 2$	$7.31 + 1$	$2.66 + 1$	$1.44 + 1$	$7.94 + 0$
20	—	—	—	$3.47 + 1$	$1.47 + 1$	$7.49 + 0$	$4.71 + 0$
40	—	—	—	$2.63 + 0$	$4.84 + 0$	$6.93 + 0$	$5.98 + 0$
60	—	—	—	$1.84 + 0$	$2.59 + 0$	$3.47 + 0$	$3.71 + 0$
80	—	—	—	$1.54 + 0$	$1.77 + 0$	$2.04 + 0$	$2.24 + 0$
100	$5.45 + 1$	$3.38 + 1$	$2.78 + 0$	$1.33 + 0$	$1.35 + 0$	$1.44 + 0$	$1.67 + 0$
120	$3.43 + 1$	$2.47 + 1$	$4.04 + 0$	$1.70 + 0$	$1.31 + 0$	$1.27 + 0$	$1.31 + 0$
160	$2.56 + 1$	$2.11 + 1$	$4.79 + 0$	$2.10 + 0$	$1.33 + 0$	$1.19 + 0$	$9.62 - 1$
200	$1.77 + 1$	$1.74 + 1$	$4.23 + 0$	$2.33 + 0$	$1.42 + 0$	$1.10 + 0$	$8.92 - 1$
240	$1.49 + 1$	$1.62 + 1$	$3.68 + 0$	$2.36 + 0$	$1.49 + 0$	$1.10 + 0$	$8.91 - 1$

^aRead as 1.48×10^5

Table 22. Dose Rate Measured in the LIC Configuration of $D = 50$ cm
($\text{mR} \times \text{h}^{-1} \times \text{MW}^{-1}$)

Z (cm)	X (cm)						
	0	20	40	60	80	100	120
20	$1.68 + 5^a$	$2.44 + 4$	$4.18 + 2$	$1.39 + 2$	$6.64 + 1$	$3.62 + 1$	$2.28 + 1$
40	$1.58 + 5$	$5.42 + 4$	$5.45 + 2$	$1.40 + 2$	$5.02 + 1$	$2.39 + 1$	$1.43 + 1$
60	—	—	—	$1.94 + 1$	$4.71 + 1$	$2.18 + 1$	$1.20 + 1$
80	—	—	—	$3.46 + 0$	$1.76 + 1$	$2.42 + 1$	$1.47 + 1$
100	—	—	—	$2.69 + 0$	$4.97 + 0$	$1.33 + 1$	$1.71 + 1$
120	$5.13 + 1$	$3.19 + 1$	$1.97 + 0$	$1.86 + 0$	$2.57 + 0$	$5.36 + 0$	$9.47 + 0$
140	$4.08 + 1$	$2.86 + 1$	$3.54 + 0$	$1.98 + 0$	$2.14 + 0$	$3.13 + 0$	$5.95 + 0$
160	$3.14 + 1$	$2.50 + 1$	$4.53 + 0$	$2.09 + 0$	$1.91 + 0$	$2.23 + 0$	$3.17 + 0$
200	$1.98 + 1$	$1.99 + 1$	$4.77 + 0$	$2.57 + 0$	$1.93 + 0$	$1.77 + 0$	$1.76 + 0$
240	$1.55 + 1$	$1.56 + 1$	$4.78 + 0$	$2.97 + 0$	$1.86 + 0$	$1.53 + 0$	$1.41 + 0$

^aRead as 1.68×10^5

Table 23. Dose Rate Measured in the LIC Configuration of D = 90 cm
(mR × h⁻¹ × MW⁻¹)

Z (cm)	X (cm)						
	0	20	40	60	80	100	120
20	1.41 + 5 ^a	2.46 + 4	3.01 + 2	1.14 + 2	6.77 + 1	4.43 + 1	3.12 + 1
40	1.38 + 5	4.57 + 4	4.95 + 2	1.66 + 2	8.40 + 1	4.73 + 1	3.02 + 1
60	1.28 + 5	4.32 + 4	6.43 + 2	2.31 + 2	9.60 + 1	5.14 + 1	2.84 + 1
80	1.20 + 5	5.60 + 4	5.81 + 2	1.64 + 2	8.02 + 1	3.74 + 1	2.18 + 1
100	—	—	—	5.12 + 1	7.09 + 1	3.54 + 1	2.30 + 1
120	—	—	—	6.82 + 0	5.42 + 1	4.11 + 1	2.29 + 1
140	—	—	—	3.67 + 0	2.44 + 1	4.35 + 1	2.95 + 1
160	4.34 + 1	3.72 + 1	2.51 + 0	2.50 + 0	7.32 + 0	2.61 + 1	2.67 + 1
180	3.81 + 1	2.98 + 1	4.74 + 0	2.68 + 0	4.36 + 0	1.42 + 1	2.26 + 1
200	3.18 + 1	2.52 + 1	5.95 + 0	3.14 + 0	3.11 + 0	7.56 + 0	1.54 + 1
240	2.15 + 1	2.11 + 1	5.65 + 0	3.45 + 0	3.06 + 0	3.67 + 0	5.37 + 0

^aRead as 1.41 × 10⁵

Table 24. Dose Rate Measured in the Configuration of No Shield in
the Cavity with the Rear Door Closed (mR × h⁻¹ × MW⁻¹)

Z (cm)	X (cm)						
	0	20	40	60	80	100	120
20	1.45 + 5 ^a	3.76 + 4	1.59 + 2	3.73 + 1	2.00 + 1	1.54 + 1	1.41 + 1
40	1.30 + 5	4.26 + 4	3.02 + 2	8.53 + 1	3.78 + 1	2.35 + 1	1.78 + 1
80	1.11 + 5	5.17 + 4	4.34 + 2	1.56 + 2	7.72 + 1	4.57 + 1	2.99 + 1
120	9.71 + 4	5.84 + 4	5.69 + 2	1.88 + 2	9.51 + 1	5.76 + 1	4.15 + 1
160	8.42 + 4	5.70 + 4	6.10 + 2	2.00 + 2	1.11 + 2	7.37 + 1	5.43 + 1
200	7.52 + 4	5.53 + 4	6.63 + 2	2.46 + 2	1.12 + 2	7.73 + 1	5.60 + 1
240	7.04 + 4	5.31 + 4	6.47 + 2	2.55 + 2	1.11 + 2	7.55 + 1	5.21 + 1

^aRead as 1.45 × 10⁵

Table 25. Dose Rate Measured in the Configuration of No Shield in
the Cavity with the Rear Door Open (mR × h⁻¹ × MW⁻¹)

Z (cm)	X (cm)						
	0	20	40	60	80	100	120
20	1.39 + 5 ^a	3.51 + 4	1.49 + 2	2.40 + 1	8.69 + 0	4.78 + 0	2.98 + 0
40	1.26 + 5	4.20 + 4	2.67 + 2	7.04 + 1	2.19 + 1	1.10 + 1	6.46 + 0
80	1.09 + 5	4.98 + 4	4.24 + 2	1.37 + 2	6.25 + 1	2.60 + 1	1.56 + 1
120	9.84 + 4	5.64 + 4	4.84 + 2	1.44 + 2	6.60 + 1	4.09 + 1	2.19 + 1
160	8.61 + 4	5.71 + 4	5.10 + 2	1.51 + 2	7.79 + 1	4.00 + 1	2.75 + 1
200	7.66 + 4	5.35 + 4	5.38 + 2	1.55 + 2	8.53 + 1	4.09 + 1	3.44 + 1
240	7.02 + 4	5.11 + 4	5.47 + 2	1.72 + 2	8.50 + 1	4.84 + 1	3.73 + 1

^aRead as 1.39 × 10⁵

mental error is comparatively large at the measurement positions on the lines $X = 0$ and 20 cm and it is 29 percent in front of the shield and 20 to 24 percent behind the shield. At other positions, it is 14 to 18 percent except at the position of $Z = 20$ cm and $X = 120$ cm where it is about 30 percent.

As shown in Fig. 15, gamma rays in the cavity may be divided into the following components. (1) penetrated through the shield, (2) leaked through the side of the shield, (3) reflected at the incident surface of the shield and streaming the space in front of the shield, (4) scattered at the inner surface of the incident hole, and (5) multi-scattered in the cavity of which sources are (1)-(4) components. Of course, this separation is not rigorous, however, it is quite convenient to use these components for the explanation of phenomena in the cavity.

Z-directional gamma-ray dose rate distributions measured behind the shield are shown in Fig. 16. For the same arrangement of shield slabs, dose rates behind the shield hardly depend on the shield location. Since the

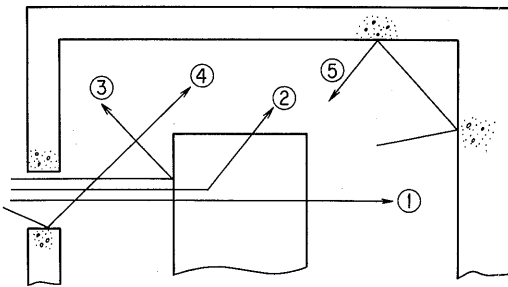


Fig. 15 Five components of gamma rays in the cavity. (1) penetration (2) leakage (3) reflection (4) scattered (5) multi-scattered.

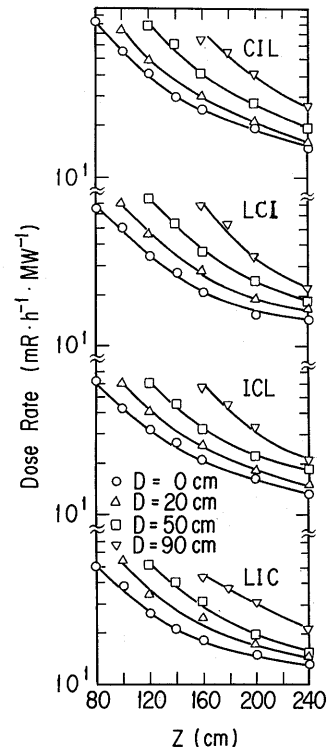


Fig. 16 Z-directional dose rate distributions measured on the line of $X = 0$ cm behind the shield.

amount of the component (5) must be affected by the change of the gap width D , it can be said that negligible small amount of the component (5) exists in this territory. Therefore dose rates behind the shield are mainly determined by the component (1). Consequently, it is concluded that the better shielding effect for the penetration component can be obtained by arranging the heavier materials to the source side. That is, the best shielding effect is found in the LIC arrangement and the worst is found in the CIL arrangement.

In general, for incident gamma rays having energies below about 2 MeV, the better shielding effect can be obtained by setting lighter materials to the source side. For gamma rays of 3 to 4 MeV, the effect of the arrangement of materials on the shielding effect is small. For higher energies, the better shielding effect is obtained by arranging the heavier materials to the source side like this experiment.

In this experiment, energies of incident gamma rays distribute up to about 8 MeV and the energy spectrum has a peak at about 8 MeV. Therefore, it is inferred that the attenuation rate of the component (1) is determined by the 8 MeV gamma rays. In order to make clear this inference, calculations were carried out using the PALLAS one-dimensional transport code. Although the actual phenomenon is two-dimensional, one-dimensional calculations are considered useful to examine the spectrum in the shield

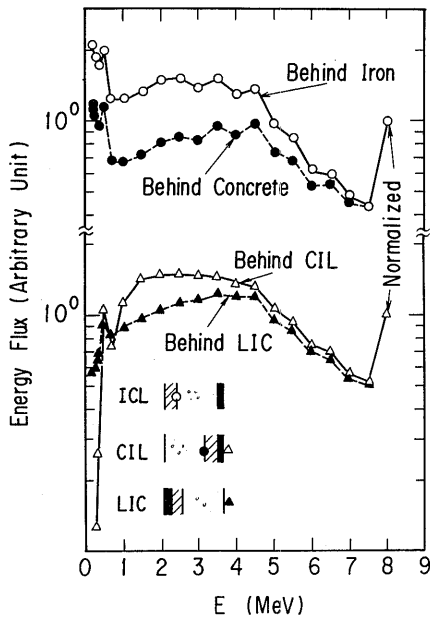


Fig. 17 Comparison of spectra calculated in and behind the shield of the ICL, CIL, and LIC arrangements.

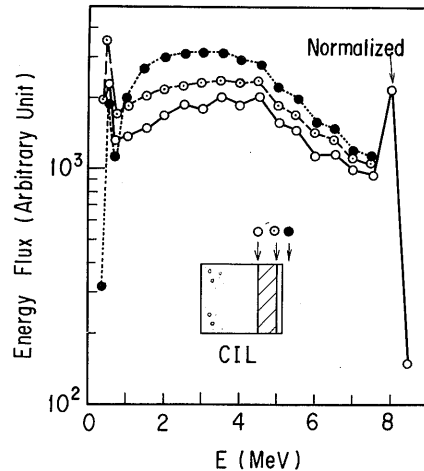


Fig. 18 Comparison of spectra calculated at each boundary of the CIL arrangement.

qualitatively. Furthermore, the effect of the bremsstrahlung can be calculated by this code. Calculations were carried out for 43 energy points between 8.5 and 0.0459 MeV. Spatial intervals are 0.5, 1.5, and 5.0 cm for lead, iron, and concrete, respectively. Sixteen angular mesh points are taken on a hemisphere.

Spectra obtained in and behind the shield of the ICL, CIL, or LIC arrangement are compared in Fig. 17. Softer spectra are seen behind heavier materials and behind the shield in which lighter materials are on the source side. Relative spectra at each boundary of the CIL arrangement are shown in Fig. 18. In the figure, spectra are normalized at 8 MeV. The spectrum becomes softer with penetrating through heavier materials. Relative dose rates calculated behind the shields for four arrangements are 1.0, 1.04, 1.12, and 1.11 for the LIC, ICL, LCI, and CIL arrangement, respectively. These results explain experimental results qualitatively fairly well, however, differences among calculated dose rates for four arrangements are much smaller than those obtained by measurements. Meanwhile, the effect of the bremsstrahlung on dose rates behind the shield were 6 percent for the ICL and CIL arrangement, 3 percent for the LCI arrangement, and 1 percent for the LIC arrangement, respectively. Note that the last slab is lead in the former two arrangements.

In Fig. 19, the dose rate distributions on the line $X = 60$ cm are compared among four arrangements of $D = 50$ cm to examine the leakage component in the side of the shield. Large differences are seen in the region of $60 \text{ cm} < Z < 120 \text{ cm}$, which is due to the difference of the shield arrangement. The dose rates in this region are superposition of the components (2), (4), and (5). Since it is difficult to separate the components (2) and (4) from the present experimental data, the component (4) is included in the component (2) in this discussion, and both are treated as the leakage component. Note that it will be shown in the next chapter that the component (4) is dominant in the side of the shield. Differences among distributions seen in Fig. 19 must be smaller than those found among distributions composed by the component (2) only. Actually, larger differences are found between the leakage components in the LIC and CIL configurations of $D = 0$ cm for which the component (5) is considered much less comparing with the cases of $D = 50$ cm. (see Fig. 10) Meanwhile the energy of gamma rays incident on the shield with the energy of 8 MeV becomes about 1.4 MeV after scattered to the direction of 45 degree. Thus, the energy distribution of the leakage component shifts to lower energy region remarkably. Therefore, one can get effective shields for high energy gamma rays by setting heavy materials to the source side.

X-directional dose rate distributions in front of the shield are shown in Fig. 20. In the case of $D = 50$ or 90 cm, dose rates are almost independent on the shield arrangement. In the case of $D = 20$ cm, dose rates are larger for

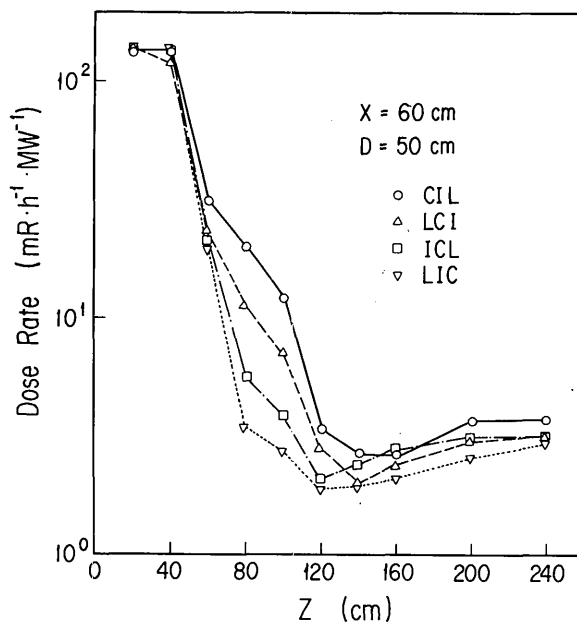


Fig. 19 Comparison of dose rate distributions measured on the line $X = 60$ cm in four configurations of $D = 50$ cm.

the arrangement with lighter materials on the source side. Let R be the distance between the measurement point and the center of the incident surface of the shield and θ be the angle between the Z -axis and the line intersecting the measurement point and the center of the incident surface of the shield as shown in Fig. 20. Then, dose rate distributions can be fairly well expressed with curves determined by $\cos \theta / R^2$. This indicates that the distributions are determined by the gamma rays reflected at the incident surface of the shield. Therefore the dose rate D at each measurement point can be calculated with the following formula,

$$D = \left(\sum \frac{D_{o_i} \times a_i}{R^2} \right) \times S ,$$

where D_{o_i} and a_i are the dose rate of incident gamma rays and the differential dose albedo of the i -th energy group, respectively, and S is the cross section of the incident hole. The dose rate D_{o_i} for each energy group was calculated with the measured spectrum given in Table 4. Then, each dose rate D_{o_i} was multiplied by 0.82 to make a correction to the decreasing gamma-ray dose rate in the radial direction on the incident surface. Differential dose albedos were calculated with Chilton and Huddreston's formula.⁽⁷⁾ The constants in this formula are given at 0.2, 0.662, 1.0, 2.5, and 6.13 MeV, respectively.⁽⁸⁾ Therefore, boundary energies of five energy groups were taken at 0, 0.4, 0.8, 1.2, 3.5, and 8.5 MeV, respectively.

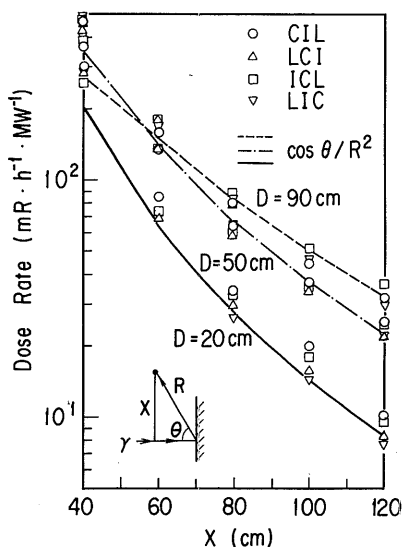


Fig. 20 X-directional dose rate distributions measured in front of the shield.

Dose rates in front of the shield are determined by the components (3), (4), and (5). The contribution of the component (4) can be approximately estimated with the measurement for the configuration of which no shield in the cavity and the rear door is open. In this territory, the main contribution of the component (5) is considered due to the gamma rays penetrating through the shield and then reflected at the rear wall. This contribution can be estimated with the difference of doses measured in the two configurations in which no shield in the cavity with the rear door open or closed. This amount resulted in negligible small at measurement positions in front of the shield. Thus, dose rates corresponding to the component (3) were obtained by eliminating only the contribution of the component (4) from measured dose rates. They are shown in Figs. 21-23 by comparing with calculations based on the above formula.

Since the first slabs of the CIL and ICL arrangement are thick enough from the point of view of albedo, calculations using the albedos of concrete and iron can be considered corresponding to the measurements for the CIL and ICL arrangement, respectively. Actually, these calculations agree well with measurements except X-40 cm for D = 90 cm where the component (4) is probably included in measured values. Large differences are seen between the measurements for the LCI and LIC arrangement and the calculations using the albedo of lead. It may be said that underestimations occur at reflection angles less than about 82 deg. where experimental results are close to calculations for concrete or iron which is the second layer of the LCI or

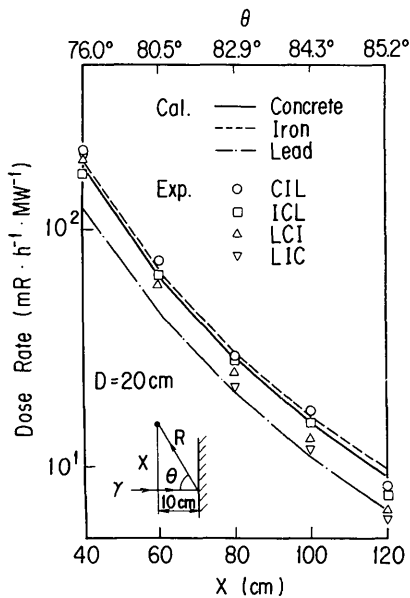


Fig. 21 Comparison of measured and calculated X-directional dose rate distributions in front of the shield placed 20 cm from the front wall.

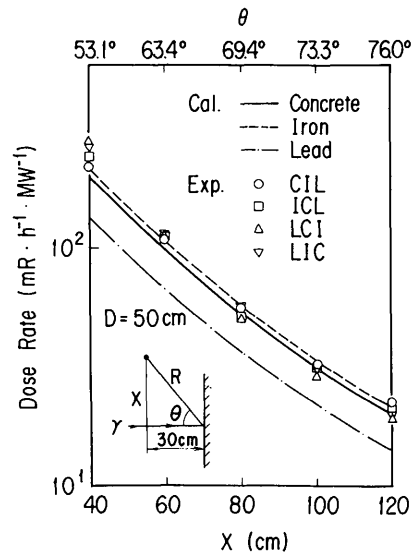


Fig. 22 Comparison of measured and calculated X-directional dose rate distributions in front of the shield placed 50 cm from the front wall.

LIC arrangement. The front lead slab in the LCI or LIC arrangement is 2.5 cm in thickness which is too thin to calculate the reflection from the LCI or LIC shield using the albedo of lead. Therefore, the effect of the second layer must be included in the calculations for the LCI or LIC arrangement. Good agreement is seen at reflection angles above about 82 deg., that is, $X > 60$ cm for $D = 20$ cm. This is probably due to large slant paths in lead at large reflection angles. For example, the slant path in lead is 15.1 cm at 80.5 deg. and increases to 20.2 cm at 82.9 deg. Thus, the 2.4 deg. increase of reflection angle turn out the 5.1 cm increase of the slant path, and experimental results become closer to the calculated values rapidly.

From these analysis, it can be concluded that the dose rate distribution in the region of $X > 40$ cm in front of shield is determined mainly by gamma rays reflected from the front surface of the shield. In this experiment, the streaming component due to multi-scattering between the front wall and the shield is not a main component. Good agreement between calculations and measurements indicates that Chilton and Huddreston's data are accurate enough to use them in this type of simple calculations.

Dose rate distributions on the line $X = 120$ cm for six CIL arrangements are shown in Fig. 24. In the figure, a peak is found that seems to move from

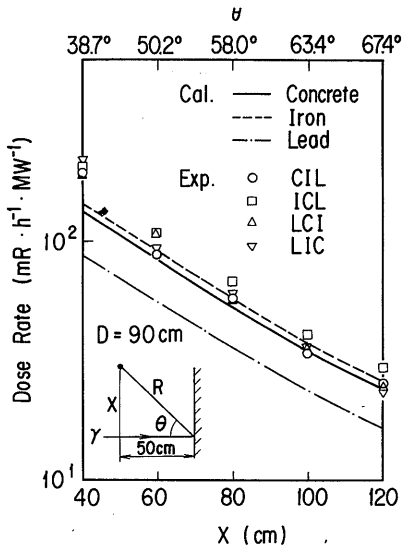


Fig. 23 Comparison of measured and calculated X-directional dose rate distributions in front of the shield placed 90 cm from the front wall.

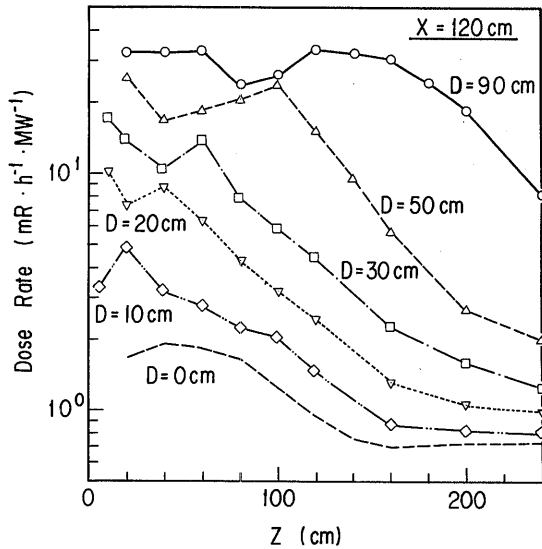


Fig. 24 Dose rate distributions measured on the traverse $X = 120$ cm in CIL configurations in which the shield is placed D cm from the front wall.

the incident hole to the slant direction. This is the component (4) which plays important role in the calculation described in the next chapter.

4. CALCULATIONS

For two CIL configurations having the gap width $D = 50$ or 90 cm, calculations were carried out using the PALLAS two-dimensional discrete ordinates transport code⁽⁹⁾ and the MORSE Monte Carlo code.⁽¹⁰⁾ PALLAS calculations in two-dimensional RZ geometries were performed for the case of $D = 50$ cm only. A geometrical model taken in calculations is shown in Fig. 25. The origin of the coordinates was taken at the core center where a point source was placed. R-directional dimensions of the shield and the concrete cavity were determined so as to conserve actual geometrical cross sections. Thus, a cylindrical shield with a radius of 56 cm was placed in a cylindrical cavity with a radius of 147 cm. The front wall and three iron slabs were replaced by a 35-cm-thick concrete wall to keep the length of the lead lining of the incident hole, since it was found, through calculations, that the gamma rays reflected at the lead lining play important role in the determination of dose rate distributions in the cavity.

To express the R-directional distribution of incident gamma rays, two types of absorbers were placed at the location corresponding to the outlet of

the experimental hole as shown in Fig. 25. The outer absorber is a "black" one which absorbs all gamma rays incident on it and the inner absorber is a "gray" one which absorbs only 36 percent of gamma rays incident on it. These two absorbers reproduced the radial distribution of the incident gamma rays fairly well as shown in Fig. 26 with dotted lines.

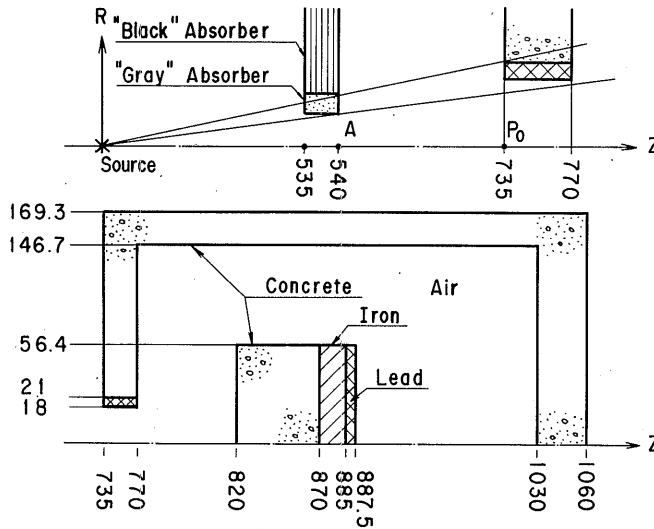


Fig. 25 Geometrical model used in PALLAS calculations. Dimensions are in centimetres.

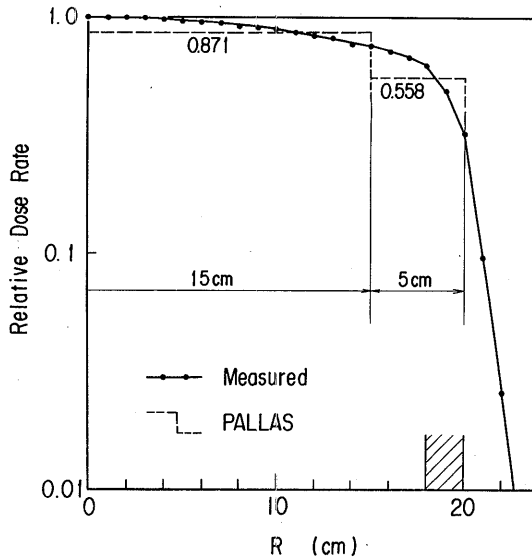


Fig. 26 X-directional dose rate distribution reproduced in PALLAS calculations.

Calculations were carried out from 8.25 MeV to 92 keV with 30 energy mesh points and with 28 angular mesh points taken on a hemisphere of which polar angles are given in Table 26. Comparisons of measured and calculated dose rate distributions on Z-directional traverses are shown in Figs. 27 and 28. Good agreement is found in front of the shield except on a line of $X = 20$ cm where a steep gradient of dose rates is seen in the X-direction. Good agreement is also seen behind the shield. However, large inconsistencies are found in the side air region of the shield. There are unrealistic peaks in the calculations. It seems that a peak moves from the incident hole to the direction corresponding to the angle θ_3 in Table 26. Therefore it was expected that this is due to the ray-effect arising from inaccurate treatment of the gamma rays scattered at the incident hole.

If this inference is true, this problem will be solved by calculating uncollided gamma rays from the incident hole analytically. Then, calculations

Table 26. Polar Angles of the Angular Quadrature Set Used in PALLAS Calculations

i	θ_i (deg.)
1	7.068
2	24.253
3	50.318
4	77.338

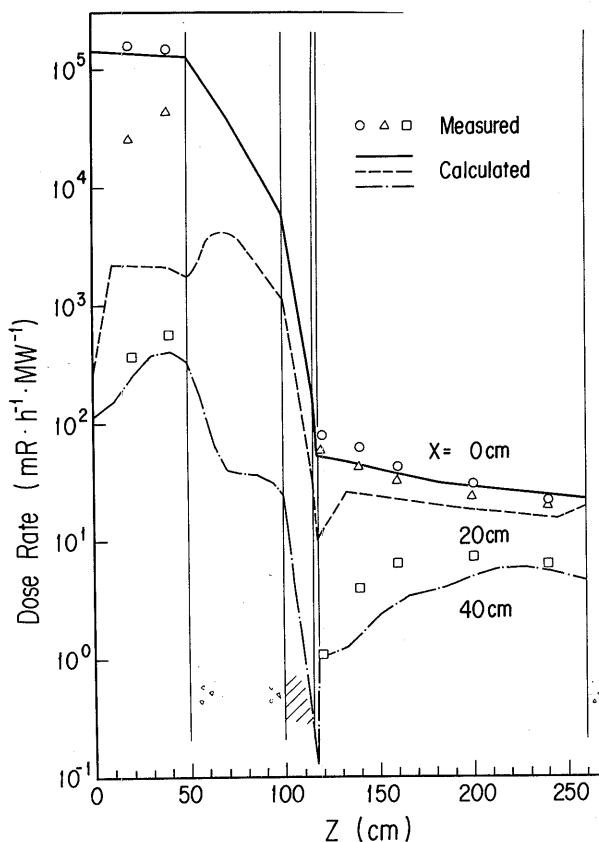


Fig. 27 Comparison of measured and calculated dose rate distributions on Z-directional traverses in the CIL configuration of $D = 50$ cm.

were divided geometrically into two steps. In the first step, calculations were carried out from the source to the inner surface of the front wall. In the second step, the boundary fluxes obtained by the first calculations were treated as the source from which uncollided gamma rays were calculated analytically. As shown in Fig. 29, an improvement is seen in calculated results. Therefore, the above inference on the ray-effect is acceptable and the method applied in the second calculations is effective to improve the calculational accuracy.

In these calculations, incident gamma rays were divided into two components, that is, one entering into the cavity without interacting with the materials of the front wall and the other mainly scattered at the incident hole. Dose rate distributions due to the two components are shown in Fig. 30, which indicates that the scattered gamma rays at the inner surface of the incident hole play important role in the determination of the dose rates on the traverse of $X = 60$ cm. Consequently, it is quite important to pay attention to the scattered gamma rays at the duct outlet in this kind of problem.

Monte Carlo calculations were carried out for two CIL configurations of

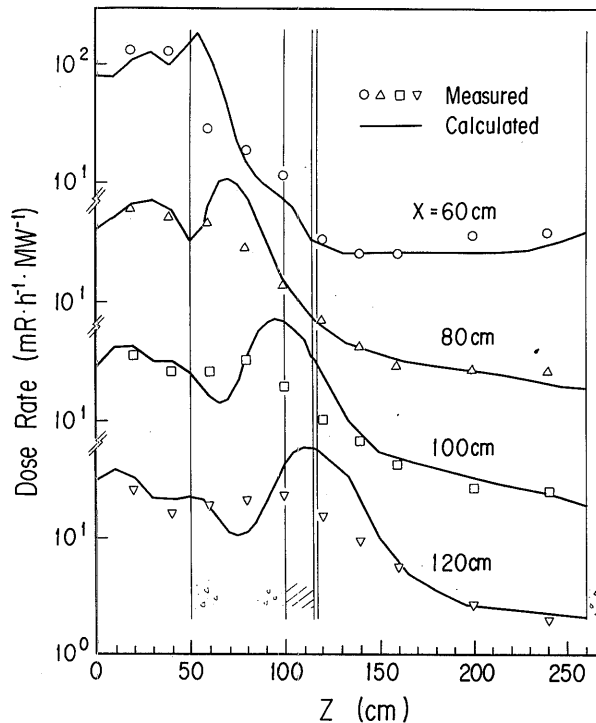


Fig. 28 Comparison of measured and calculated dose rate distribution on Z-directional traverses in the CIL configuration of $D = 50$ cm.

$D = 50$ cm and 90 cm. Accurate geometrical models were taken. Incident gamma rays were emitted from a disk source of 40 cm in diameter placed at the position P_0 . They were sampled uniformly in a cone having an opening angle of 5 deg. around the axis. The radial distribution of measured incident gamma rays was accurately reproduced in calculations. The DLC-23 cross section file was used, so that P_3 calculations were carried out with 18 energy groups of which boundary energies are given in Table 27. The number of histories were chosen so that fractional standard deviations would be less than 0.1 , which resulted in about five thousands.

Comparisons of measured and calculated results in front of and behind the shield are shown in Fig. 31 for $D = 50$ cm and Fig. 32 for $D = 90$ cm. Fairly good agreement is found in these areas except on the line $X = 20$ cm where extremely steep gradient of dose rates are seen. Comparisons of measured and calculated results in the side of the shield are shown in Fig. 33 for $D = 50$ cm and Fig. 34 for $D = 90$ cm. In spite of fairly good agreement seen in the case of $D = 50$ cm, rather large disagreements are found in the case of $D = 90$ cm. As a cause of these disagreements, inaccurate treatment

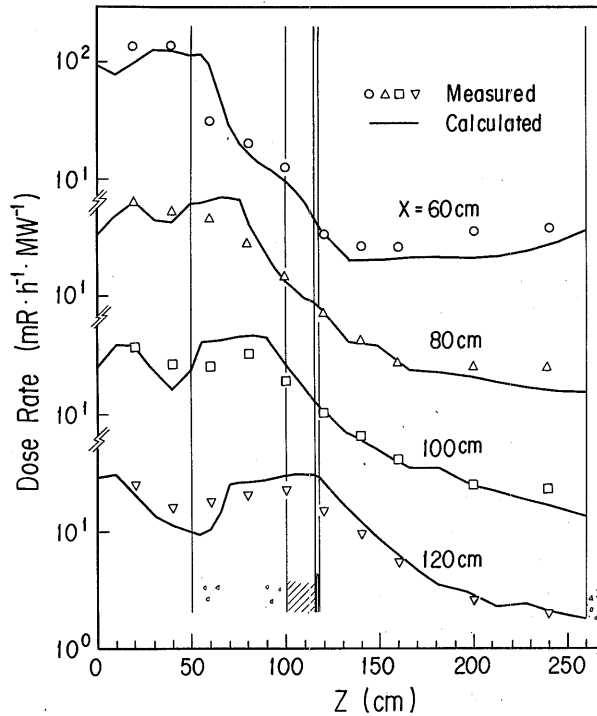


Fig. 29 Comparison of measured and calculated dose rate distributions on Z-directional traverses. Uncollided fluxes are calculated analytically.

of photon scattering with P_3 cross sections is considered. In these figures, only fractional standard deviations larger than 0.2 are indicated.

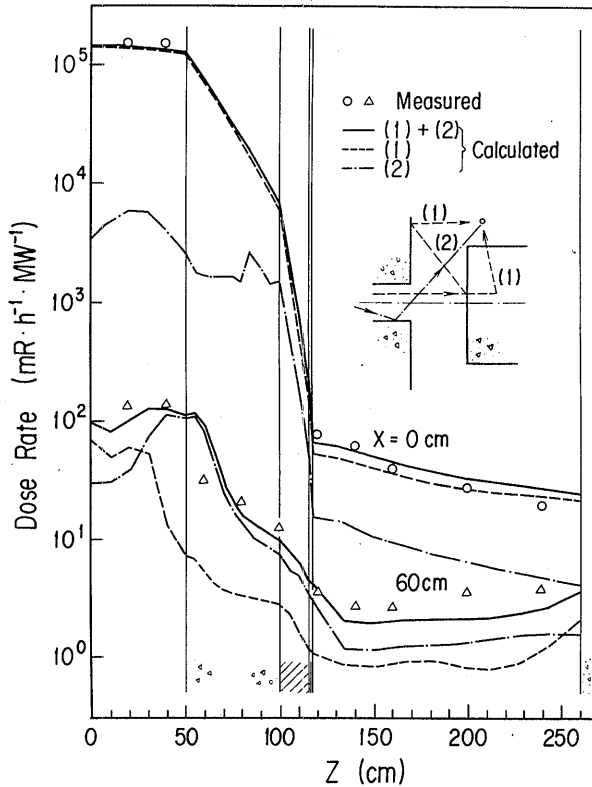


Fig. 30 Calculated dose rate distributions due to the two components of incident gamma rays.

Table 27. Energy Group Structure of MORSE Calculations

Group No.	Energy Range (MeV)	Group No.	Energy Range (MeV)
1	1.00 + 01 ^a — 8.00 + 00	10	1.33 + 00 — 1.00 + 00
2	8.00 + 00 — 6.50 + 00	11	1.00 + 00 — 8.00 - 01
3	6.50 + 00 — 5.00 + 00	12	8.00 - 01 — 6.00 - 01
4	5.00 + 00 — 4.00 + 00	13	6.00 - 01 — 4.00 - 01
5	4.00 + 00 — 3.00 + 00	14	4.00 - 01 — 3.00 - 01
6	3.00 + 00 — 2.50 + 00	15	3.00 - 01 — 2.00 - 01
7	2.50 + 00 — 2.00 + 00	16	2.00 - 01 — 1.00 - 01
8	2.00 + 00 — 1.66 + 00	17	1.00 - 01 — 5.00 - 02
9	1.66 + 00 — 1.33 + 00	18	5.00 - 02 — 1.00 - 04

^aRead as 1.00×10^1

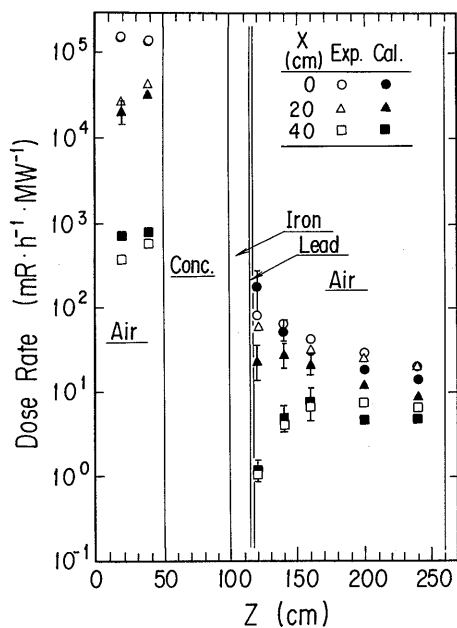


Fig. 31 Comparison of measured and calculated dose rate distributions on Z-directional traverses in the CIL configuration of $D = 50$ cm.

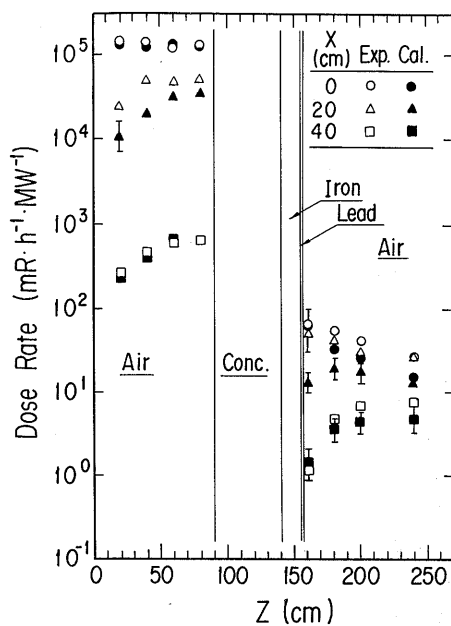


Fig. 32 Comparison of measured and calculated dose rate distributions on Z-directional traverses in the CIL configuration of $D = 90$ cm.

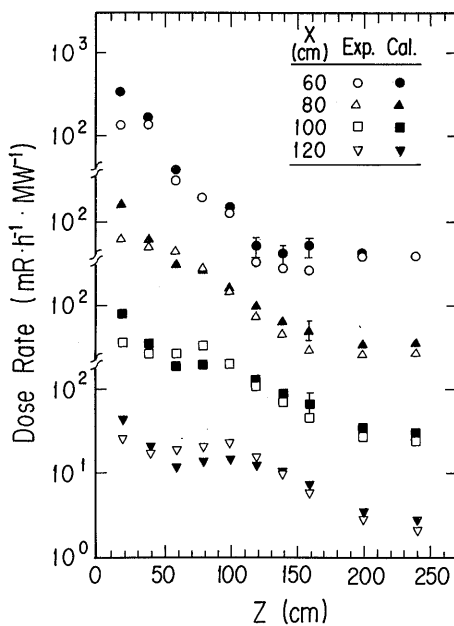


Fig. 33 Comparison of measured and calculated dose rate distributions on Z-directional traverses in the CIL configuration of $D = 50$ cm.

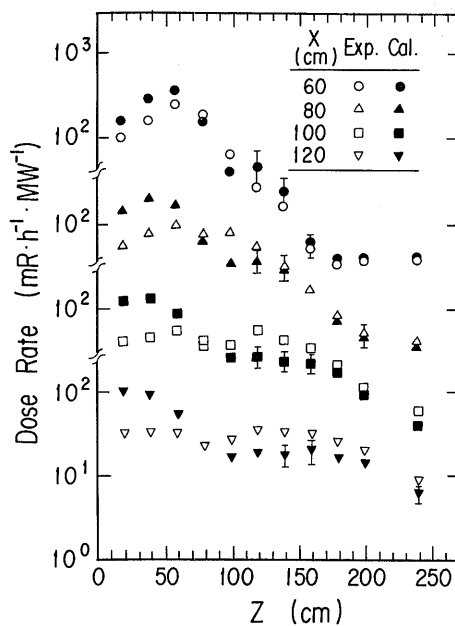


Fig. 34 Comparison of measured and calculated dose rate distributions on Z-directional traverses in the CIL configuration of $D = 90$ cm.

5. CONCLUSION

The following conclusions are obtained from the analysis of experimental data on the shield for leakage gamma rays from a duct.

1. For the penetration component, a better shielding effect can be obtained by setting heavier materials to the source side.
2. The same conclusion is obtained for the leakage component.
3. The reflection component can be calculated by using a simple formula and Chilton and Huddreston's albedo data.
4. The gamma rays scattered at the inside of the duct outlet play important role in the problem of additional shield.

Experimental data obtained for twenty shield configurations can be used to assess calculations of the effect of additional shields for leakage gamma rays from ducts. In calculations with the discrete ordinates transport code PALLAS, the ray-effect was found in the case of straight forward calculations because of inaccurate treatment of gamma rays scattered at the duct outlet. This problem was solved by performing analytical calculations for gamma rays scattered at the duct outlet and going to detection points without any collisions. Monte Carlo calculations with the MORSE code gave fairly good results in the configuration of $D = 50$ cm, however, large disagreements were found between measured and calculated results in the configuration of $D = 90$ cm. The cause of the disagreement was not clarified in this study, however, it was considered that one of the reasons is inaccurate treatment of photon scattering with P_3 cross sections.

ACKNOWLEDGEMENT

This work is a part of the cooperative research of the Ship Research Institute and the JAERI on the shielding of a marine reactor.

The authors wish to express their thanks to the personnel of JRR-4 for reactor operation.

REFERENCES

- 1) T.Miura, K. Takeuchi, and M. Kinno, Study on Additional Shields for Gamma-Rays Streaming Through a Duct, Proc. 6th Int. Conf. radiation shielding, 2, 787 (1983)
- 2) S. Miyasaka, A User's Manual for JRR-4 Experimental Facilities, JAERI 6016, (1965) (in Japanese)
- 3) K. Saito, and S. Moriuchi, Monte Carlo Calculation of Accurate Response Functions of a NaI(Tl) Detector for Gamma Rays, Nucl. Instrum. Methods, 185, 299 (1981)
- 4) T. Miura, Assessment of Data and Methods to Form Response Functions of a 3'' ϕ x 3'' NaI(Tl) Detector, Nucl. Instrum. Methods, 221, 603 (1984)
- 5) W.R. Burrus and V.V. Verbinski, Fast Neutron Spectroscopy with Thick Organic Scintillators, Nucl. Instrum. Methods, 67, 181 (1969)
- 6) K. Takeuchi, S. Tanaka, and M. Kinno, Transport Calculation of Gamma Rays Including Bremsstrahlung by the Discrete Ordinates Code PALLAS, Nucl. Sci. Eng., 78, 273 (1981)
- 7) A.B. Chilton and C.M. Huddreston, A Semiempirical Formula for Differential Dose Albedo for Gamma Rays on Concrete, Nucl. Sci. Eng., 17, 419 (1963)
- 8) A.B. Chilton, C.M. Davisson, and L.A. Beach, Parameters for C-H Albedo Formula for Gamma Rays Reflected from Water, Concrete, Iron, and Lead, Trans. Am. Nucl. Soc., 8, No. 2, 656 (1965)
- 9) K. Takeuchi, PALLAS-2DCY-FC, A Computational Method and Radiation Transport Code in Two-Dimensional (R, Z) Geometry, Papers Ship Res. Inst., No. 57 (1979)
- 10) E.A. Straker et al., The MORSE Code — A Multigroup Neutron and Gamma-Ray Monte Carlo Code, ORNL-4585, (1970)